Front. Earth Sci. 2019, 13(4): 705–720
https://doi.org/10.1007/s11707-019-0790-8

RESEARCH ARTICLE

# Numerical and experimental study of the aerodynamic characteristics around two-dimensional terrain with different slope angles

**Pingzhi FANG (✉)[1], Deqian ZHENG[2], Liang LI[2], Wenyong MA[3], Shengming TANG[1]**

1 Shanghai Typhoon Institute of China Meteorological Administration, Shanghai 200030, China
2 School of Civil Engineering and Architecture, Henan University of Technology, Zhengzhou 450001, China
3 Wind Engineering Research Center, Shijiazhuang Tiedao University, Shijiazhuang 050043, China



**Abstract** Complicated terrain was considered and simplified as two-dimensional (2D) terrain in a dynamical downscaling model and a parametric wind field model for typhoons developed by the Shanghai Typhoon Institute. The 2D terrain was further modeled as uphill and downhill segments with various slope angles relative to the incoming flow. The wind speed ratios and pressure characteristics around the 2D terrain were numerically and experimentally investigated in this study. Aerodynamic characteristics of the 2D terrain with a limited-length upper surface were first investigated in the wind tunnel with sheared incoming flow. The corresponding numerical investigation was also conducted by using the commercial computational fluid dynamics code FLUENT with the realizable $k$-$\varepsilon$ turbulence model. Special efforts were made to maintain the inflow boundary conditions throughout the computational domain. Aerodynamic characteristics were then investigated for the ideal 2D terrain with an unlimited-length upper surface by using a numerical method with uniform incoming flow. Comparisons of the different terrain models and incoming flows from the above studies show that the wind pressure coefficients and the wind speed ratios are both affected by the slope angle. A negative peak value of the wind pressure coefficients exists at the escarpment point, where flow separation occurs, for the uphill and downhill terrain models with slope angles of 40° and 30°, respectively. Correspondingly, the streamwise wind speed ratios at the points above the escarpment point for the uphill terrain model increase with increasing slope angle, reach their peak values at the slope angle of $\alpha$ = 40° and decrease when the slope angle increases further. For the downhill terrain model, similar trends exist at the points above the escarpment point with the exception that the critical slope angle is $\alpha$ = 30°.

**Keywords** numerical simulation, wind tunnel test, aerodynamic characteristics, critical slope angle

## 1 Introduction

With the progress of studying meteorological disasters, a higher precision and finer resolution wind field is one of the basic requirements in hazard models, which inevitably involve considering finer resolution terrain. In the dynamic framework of the numerical weather prediction (NWP) model, for example, there are still many challenges in providing finer-resolution wind fields that consider the complicated or finer-resolution terrain (Wyngaard, 2004). However, downscaling technology coupled with the NWP model can avoid some problems and efficiently provide the wind field at the hundred-meter level compared to the numerical simulation based on the NWP model itself (Wilby and Wigley, 1997; Walton et al., 2015). Generally, downscaling technology can be classified into the statistical downscaling method (Fan, 2006) and the dynamical downscaling method. For the dynamical downscaling method, the finer-resolution wind field or meteorological data are derived considering the interactions among the control equations and the finer-resolution terrain, as well as the information at the coarser grids provided by the NWP model (Dickinson et al., 1989; Yang et al., 2010). The dynamical downscaling method is favored by many researchers because it possesses the advantage of physical meaning in interpreting the effects of the local terrain on the near surface wind field (Jackson and

Received April 25, 2019; accepted September 2, 2019

E-mail: freedomfpz@163.com

Hunt, 1975; Mortensen and Landberg, 1993; Wang et al., 2008).

Recently, a dynamical downscaling model and a parametric wind field model for typhoons were developed by the Shanghai Typhoon Institute. Complicated terrain was considered in the two models and simplified as two-dimensional (2D) uphill or downhill (relative to the incoming flows) with various slope angles. Aerodynamic characteristics around the 2D terrain model were thus necessary to calculate the near-surface wind field with finer resolution over the complicated terrain. Although flow around a similar 2D terrain model has been investigated by many studies (Bowen and Lindley, 1977; Kondo et al., 2002; Lun et al., 2007) and the wind speed acceleration effect around the slope can also be predicted by the prevailing standards (e.g., GB50009-2012, AIJ-2004, ASCE/SEI 7-10, NBC-2005, ISO 4354-2009 E, and AS/NZS 1170.2-2011), the corresponding results either lack wind pressure information or are only available for the uphill terrains. Hence, aerodynamic characteristics from previous studies are not comprehensive enough for the dynamical downscaling model and the parametric wind field model for typhoons.

There are generally two ways to investigate the aerodynamic characteristics over complicated terrains, i.e., the wind tunnel method and the numerical simulation. For the wind tunnel method, the aerodynamic characteristics of the terrain model are measured in the wind tunnel (Bowen and Lindley, 1977; Ishihara et al., 1999; Ishihara et al., 2001; Kondo et al., 2002; Cao and Tamura, 2006, 2007; Hu et al., 2018; Kamada et al., 2019). The numerical simulation is based on computational fluid dynamics (CFD) technology, and the aerodynamic characteristics of the terrain model are obtained by solving the Navier-Stokes (N-S) equations in a discretizing computational domain. According to the difference in the solution method to the N-S equations, there are two widely accepted CFD simulation methods, i.e., the Reynolds averaged N-S equation (RANS) method (Lun et al., 2007; Makridis and Chick, 2013; Yan et al., 2016) and the large eddy simulation (LES) method (Ishihara and Hibi, 2002; Cao et al., 2012; Liu et al., 2016). The RANS method is based on the time-averaged operation on the N-S equations; thus, only the time-averaged flow field can be obtained. Contrary to the RANS method, the N-S equations are spatially averaged in the LES method. Therefore, the LES method possesses the advantage of obtaining the fluctuating value of the flow field except that it is more time consuming than the RANS method. In the present study, only a time-averaged flow field was needed; thus, the RANS-based numerical simulation method was adopted. This was realized by the commercial CFD code FLUENT with the realizable $k$-$\varepsilon$ turbulence model.

In this paper, aerodynamic characteristics around various 2D terrain models with different incoming flows were numerically and experimentally studied. A simplified terrain model with a limited-length upper surface was presented, and a brief description of the wind tunnel test with sheared incoming flow is illustrated in Section 2. The numerical simulation method based on the commercial CFD code FLUENT was depicted with the emphasis on simulating the well-developed neutral atmospheric boundary layer in Section 3. The numerical simulation corresponding to the wind tunnel test was conducted, and the reliability of the numerical method was also validated by the experimental investigation. In Section 4, the effects of the slope angle on the aerodynamic characteristics around the ideal 2D terrain model with unlimited-length upper surface were investigated in detail with uniform incoming flow. The results of the aerodynamic characteristics around the various 2D terrain models and different incoming flows are discussed, and some conclusions are summarized in Section 5.

## 2 Terrain model and the wind tunnel test

The simplified 2D terrain model is shown in Fig. 1(a). Due to the practical difficulty in the wind tunnel test, the simplified 2D uphill or downhill terrain with various slope angles was modeled with limited length for the upper

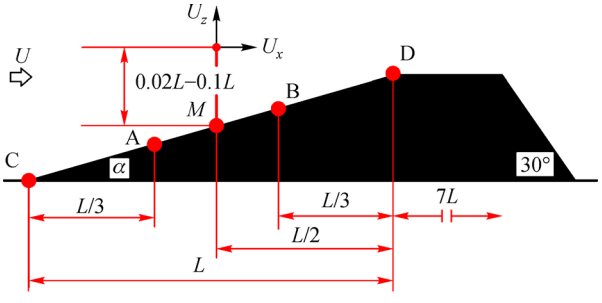


(a)

(b)

**Fig. 1** (a) Sketches of the simplified 2D uphill terrain model with a limited length-upper surface of 7$L$. Aerodynamic characteristics at 5 locations along the slope surface and 11 points over each location along the slope surface were measured; and (b) the corresponding physical model in the wind tunnel with the Cobra Probes.

surface. To avoid flow disturbance on the slope surface (i.e., the CAMBD line in Fig. 1(a)), the upper surface length was set to 7$L$ with a transition slope angle of 30° to the land surface. Here, the characteristic length $L$ is the horizontal projection length of the slope surface. The slope surface was placed to face the incoming flow for the uphill test cases, as shown in Fig. 1(a). For the downhill test cases, the slope surface was in the leeward direction (not shown here).

The wind tunnel tests (Fig. 1(b)) were carried out in the Wind Engineering Research Center of Shijiazhuang Tiedao University. The test section of the wind tunnel is 24.0 m (length) × 4.4 m (width) × 3 m (height). The maximum wind speed is up to 30 m/s in the test section, and the corresponding turbulent intensity and the difference in the wind speed distribution over the test section are both less than 0.4%. Four slope angles, i.e., $\alpha$ = 15°, 30°, 45° and 60°, were considered in the wind tunnel test, and the corresponding characteristic lengths were $L$ = 500 mm, 400 mm, 200 mm and 150 mm, respectively. The wind pressure at five locations (i.e., C, A, M, B and D) was measured along the slope surface by using the DTC Initium electronic pressure scanning system, as shown in Fig. 1(a). The streamwise and vertical wind speed ratios at 11 points (equally distributed from 0.02$L$ to 0.1$L$) over each location along the slope surface were both measured by using the Series 100 Cobra Probes. The test was placed in the wind field without the roughness elements and the spires. However, a wind profile below the height of 600 mm was developed before the test section due to the friction effect of the wind tunnel ground surface; the wind profile is marked as 'Exp' in Fig. 2. In this paper, the gradient velocity $U_g$ at the gradient height ($Z_g$ = 600 mm) was 7.4 m/s. The turbulent intensity $I_{ug}$ at the gradient height was approximately 5.8%.

## 3 Comparisons between the CFD simulation and the wind tunnel test with sheared incoming flow

### 3.1 Computational domain and the mesh scheme

The simulation results with sheared incoming flow were validated by comparison with the wind tunnel test. The present numerical simulation was conducted by adopting the commercial CFD code FLUENT (ANASYS 19). According to the guidelines provided by the AIJ (Architectural Institute of Japan) (Tominaga et al., 2008) and the COST Action 732 (2005–2009), the domain scale was set to 24000 mm × 4000 mm × 3000 mm in the streamwise, spanwise and vertical directions, respectively, considering the characteristic length $L$ of the terrain model. The domain was meshed using non-uniformly structured grids. Two mesh schemes with a vertical grid space of 1 mm were adopted for the domain to test the effects of the mesh on the computational results. The total cell numbers are approximately 1 million and 2 million for the present- and the fine-mesh scheme, respectively. Figure 3 depicts the sketches of the present-mesh scheme. In the following comparisons, the simulation results based on the two meshes were denoted as CFD1 and CFD1_F, where CFD1_F was the fine-mesh simulation result.

### 3.2 The numerical simulation method

The RANS-based realizable $k$-$\varepsilon$ turbulence model (Shih et al., 1995) was adopted in the present simulation. A Green-Gauss node-based solver was used to obtain more accurate results. SIMPLEC (Van Doormaal and Raithby, 1984) was selected for the velocity-pressure decoupled method. Second-order upwind discretization methods were

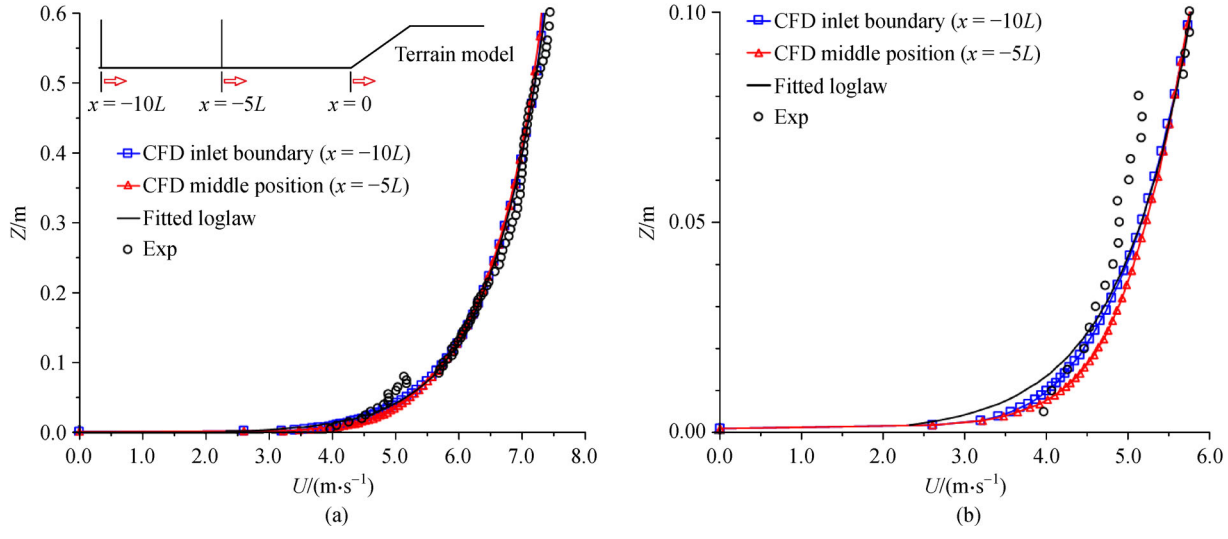


**Fig. 2** (a) Comparisons of the mean wind profiles among the wind tunnel test, fitted logarithmic law, the prescribed inlet flow at the inlet boundary ($x$ = −10$L$) and the approaching flow before the uphill terrain model ($x$ = −5$L$); and (b) comparisons near the land surface.

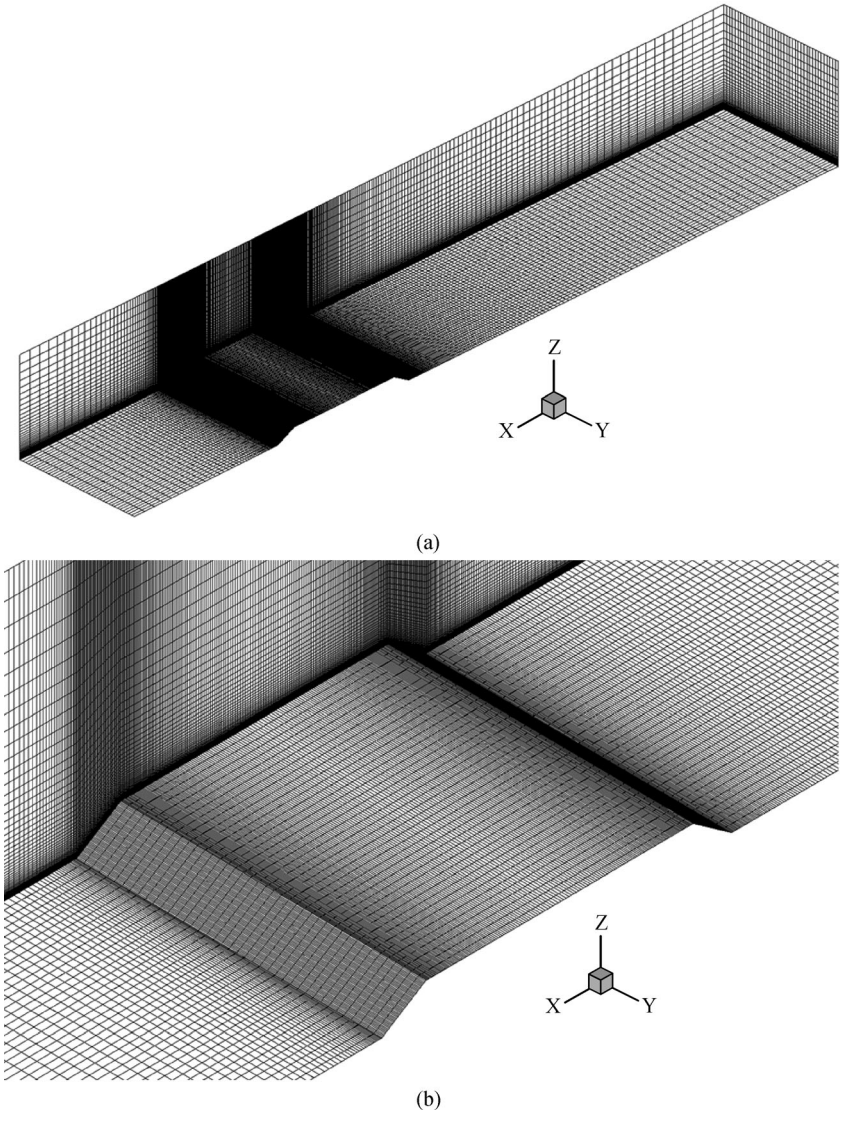


**Fig. 3** (a) Overview of the CFD domain and mesh scheme; and (b) close view of the mesh scheme around the terrain model with limited-length upper surface.

adopted for the continuity and momentum equations. The computation was stopped when the residual error curves of all the physical quantities moved without variation (less than $10.0^{-3}$). Default options were used for the rest of the setups. Velocity-inlet boundary conditions (BCs) were set for the inflow boundary of the domain. Pressure-outlet BCs were set for the outflow boundary of the domain. Symmetry BCs were used for the two sides and the top boundary of the domain. Wall BCs were adopted for the ground and the terrain model surfaces. The logarithmic wind profile, fitted by the experimental wind profile (shown in Fig. 2 as 'Fitted loglaw'), was adopted for the velocity-inlet BCs with the expression as follows:

$$\frac{U}{u_*} = \frac{1}{\kappa}\ln\left(\frac{z+z_0}{z_0}\right), \tag{1}$$

where $U$ is the velocity in the streamwise direction, $u_*$ is the friction velocity, $z$ is the height above the land surface, $\kappa$ is the Karman constant with $\kappa = 0.42$, and $z_0$ is the aerodynamic roughness length. The fitted values of $u_*$ and $z_0$ are listed in Table 1. Special efforts, briefly described below, were made for the velocity-inlet BCs to be maintained throughout the computational domain to reproduce the neutral atmospheric boundary layer (ABL) for the numerical simulation.

For the RANS-based simulation, the standard wall function proposed by Launder and Spalding (1974) was widely accepted. The wall function problem, which underlies the difference between the inlet and approaching flows, may exist in simulating the neutral ABL with a larger aerodynamic roughness length based on the standard wall function (Blocken et al., 2007). Many efforts were made on the wall function problem in modeling the neutral ABL (Juretic and Kozmar, 2014; Cindori et al., 2018). Originally, the standard wall function considers the

**Table 1** Model constants for the wind field with the realizable $k$-$\varepsilon$ turbulence model

| Wind field | | | Model constants | | |
|---|---|---|---|---|---|
| $u$/(m·s$^{-1}$) | $z_0$/m | $z_0'$/m | $C_2$ | $\sigma_e$ | $\sigma_k$ |
| 0.3752 | $1.5538 \times 10^{-4}$ | $9.7 \times 10^{-5}$ | 1.9 | 1.2 | 0.4 |

uniform roughness elements distributed regularly on the surface. However, the roughness elements on the land surface are non-uniform and are distributed irregularly. An extra term is thus necessary to resolve the wall function problem in simulating the neutral ABL (Fang et al., 2015) as follows:

$$\frac{U}{u_*} = \frac{1}{\kappa}\ln\frac{z}{K_s} + C_2 - \delta B, \tag{2}$$

where $C_2$ is the model constant with $C_2$ = 1.9, $K_s$ is the physical roughness height, and $\delta B$ is the extra term defined by $\delta B = (\ln \beta)/\kappa$. The parameter $\beta$ from $z_0' = z_0/\beta$ is often larger than 1.0, which means that the standard wall function with the extra term can produce a smaller mean wind speed and is necessary for simulating the neutral ABL with a larger value of the aerodynamic roughness length $z_0$. The above equation is reduced to the standard wall function when $\beta = 1$. The extra term can be realized by the user-defined function (UDF) in FLUENT. The turbulent model constants and all the BCs, which are necessary for maintaining the prescribed velocity-inlet BCs throughout the computational domain, are listed in Tables 1 and 2. Comparisons of the simulated wind profiles at the inflow boundary ($x = -10L$) and the approaching flow ($x = -5L$) before the terrain model are shown in Fig. 2. Despite some discrepancies with the experimental data at approximately 0.05–0.1m near the ground, good agreement can be found between the approaching flow ($x = -5L$) before the terrain model and the prescribed inlet flow ($x = -10L$) at the inflow boundary. The comparison results indicate that the present method is capable of maintaining the velocity-inlet BCs throughout the computational domain.

### 3.3 Simulation results

The wind pressure coefficients $C_{\mathrm{pi,mean}}$ at the five locations along the slope surface, and the streamwise wind speed ratios $R_{ix}$ and the vertical wind speed ratios $R_{iz}$ at points over the slope surface were all normalized by the gradient velocity $U_g$ with the expressions as follows:

$$C_{\mathrm{pi,mean}} = \frac{\delta P_i}{0.5\rho U_g^2}, \tag{3}$$

$$R_{ix} = \frac{U_{ix}}{U_g}, \tag{4}$$

$$R_{iz} = \frac{U_{iz}}{U_g}, \tag{5}$$

where $\rho = 1.225$ kg/m$^3$ is the air density, $\delta P_i$ is the dynamic pressure at location $i$, and $U_{ix}$ and $U_{iz}$ are the streamwise and the vertical mean wind speeds at point $i$, respectively.

Figures 4–6 show the comparison results of the wind pressure coefficients, the streamwise wind speed ratios and the vertical wind speed ratios between the simulation results (CFD1 & CFD1_F) and the wind tunnel data (Exp1). For simplicity, only the results from the slope angles with $\alpha$ = 15° and 30° were presented. Figure 4 shows that the simulated wind pressure coefficients coincide with the experimental data for the two slope angles, despite the difference in the estimation of wind suction at location D where flow separation exists. Good agreement is observed for the comparisons of the streamwise wind speed ratios from the uphill terrain model (Figs. 5(a) and 5(b)), while some difference is found in the vertical wind speed ratios (Figs. 5(c) and 5(d)), especially at location D, where the vertical wind speed ratios are overestimated by the present simulation. For the comparison results of the downhill terrain model shown in Fig. 6, the simulated streamwise and vertical wind speed ratios agree well with the experimental data for most points over the slope surface. For the other two cases with $\alpha = 45°$ and 60°, similar results were obtained with the exception

**Table 2** BCs for the wind field with the realizable $k$-$\varepsilon$ turbulence model

| Boundary | BC | Mathematical implication | |
|---|---|---|---|
| Inlet | Velocity-Inlet | $U$ | $\frac{U}{u_*} = \frac{1}{\kappa}\ln\left(\frac{z+z_0}{z_0}\right)$ |
| | | $k$ | $k = 1.5 \times (U_g I_{ug})^2 = 0.28 m^2/s^2$ |
| | | $\varepsilon$ | $\varepsilon = C_\mu^{1/2} k \frac{\partial U}{\partial z}$, $C_\mu = 0.09$ |
| Outlet | Pressure-Outlet | | $k$, $\varepsilon$: the same as those at the inlet boundary |
| Top | Symmetry | | $\partial(U, P, k, \varepsilon)/\partial z = 0$ |
| Side | Symmetry | | $\partial(U, P, k, \varepsilon)/\partial y = 0$ |
| Terrain surface | Wall | Standard wall function: $K_s = 0$ | |
| Land surface | Wall | User defined wall function with $\delta B = 7.0$ and $K_s = 10.0 z_0$ | |

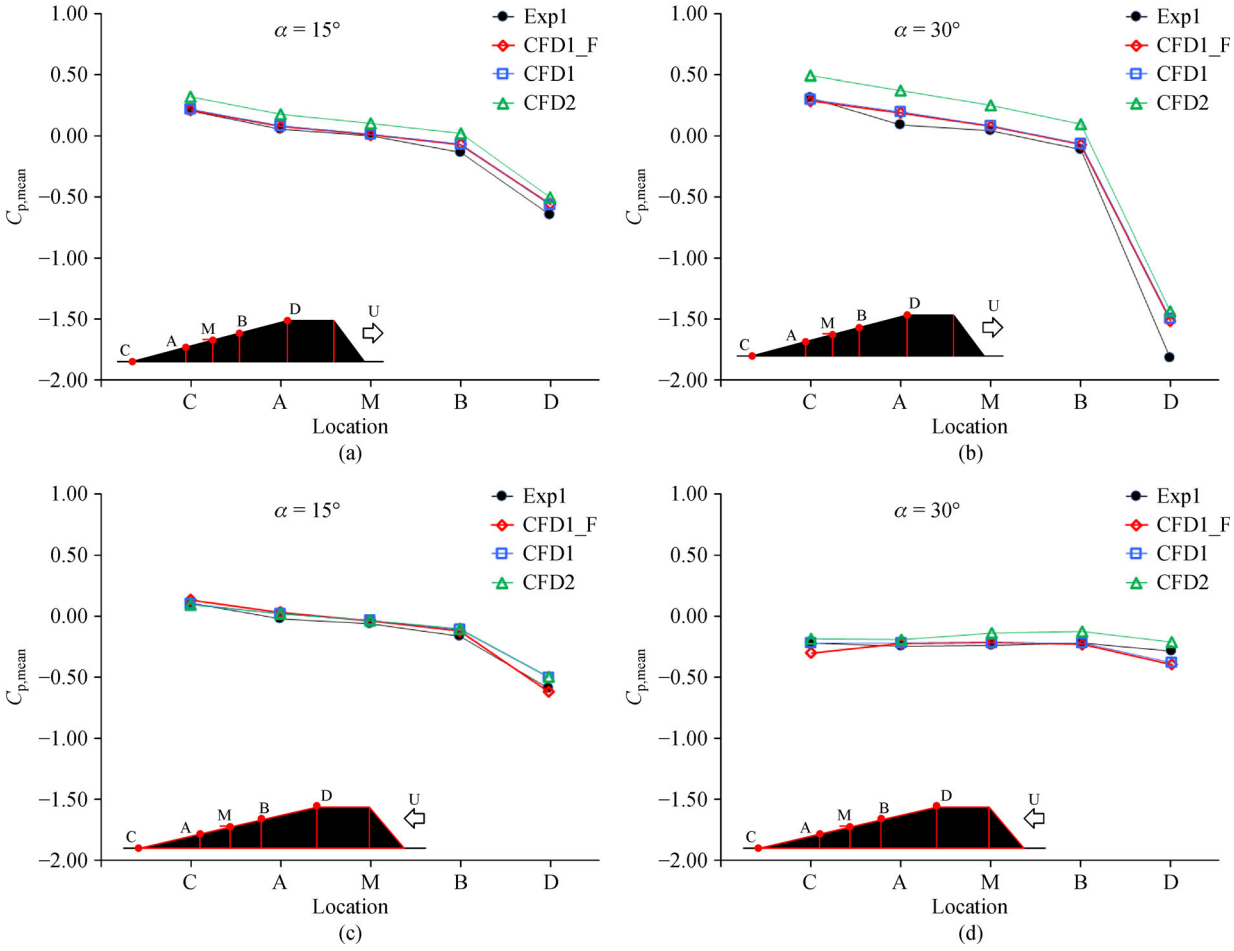


**Fig. 4** Comparisons of the mean wind pressure distribution from the terrain model with limited-length upper surface: (a) uphill model with $\alpha = 15°$; (b) uphill model with $\alpha = 30°$; (c) downhill model with $\alpha = 15°$; and (d) downhill model with $\alpha = 30°$.

that the overestimation of the vertical wind speed ratios are more obvious for the uphill terrain model. As far as the mesh scheme is concerned, there is almost no difference in the pressure coefficient distribution and the wind speed ratios between the simulation results of the two meshes (CFD1 & CFD1_F), as shown in Figs. 4–6.

Parts of the simulation results are further verified by the experimental studies (Kondo et al., 2002) and the predicted values from the prevailing standards. Figure 7 shows the comparison results of the topographic multiplier at location D for slope angles $\alpha = 15°$ and 30°. The topographic multiplier is defined as follows:

$$R'_{ix} = \frac{U_{ix}}{U(z_i)}, \tag{6}$$

where $z_i$ is the height above the uphill model surface at point $i$; $U(z_i)$ is the undisturbed mean wind speed or the inflow boundary conditions at $z_i$. It can be seen from Fig. 7 that the simulation results can basically agree with the previous experimental data (Kondo et al., 2002) and the predicted value by the prevailing standards for most points at $Z/L \geqslant 0.04$. The topographic multiplier is overestimated by the simulation results when the measuring points are relatively near the model surface. In general, the comparison results indicate that the present method is capable of simulating the flow around the terrain model.

## 4 Results from the CFD simulation with uniform incoming flow

### 4.1 Brief description of the CFD simulation

Due to the limitation of the experimental method depicted in Section 2, the wind tunnel test method can only provide aerodynamic characteristics around the 2D terrain model with limited-length upper surface and sheared incoming flow. However, aerodynamic characteristics around an ideal 2D terrain model with unlimited-length upper surface and uniform incoming flow are needed in the dynamical downscaling model and the parametric typhoon model. This can be implemented by adopting the CFD method. The domain and mesh scheme for the ideal 2D terrain model are shown in Fig. 8. The horizontal projection length $L$ of the slope surface was fixed at 500 mm. The ideal 2D terrain models with sheared incoming flow for the

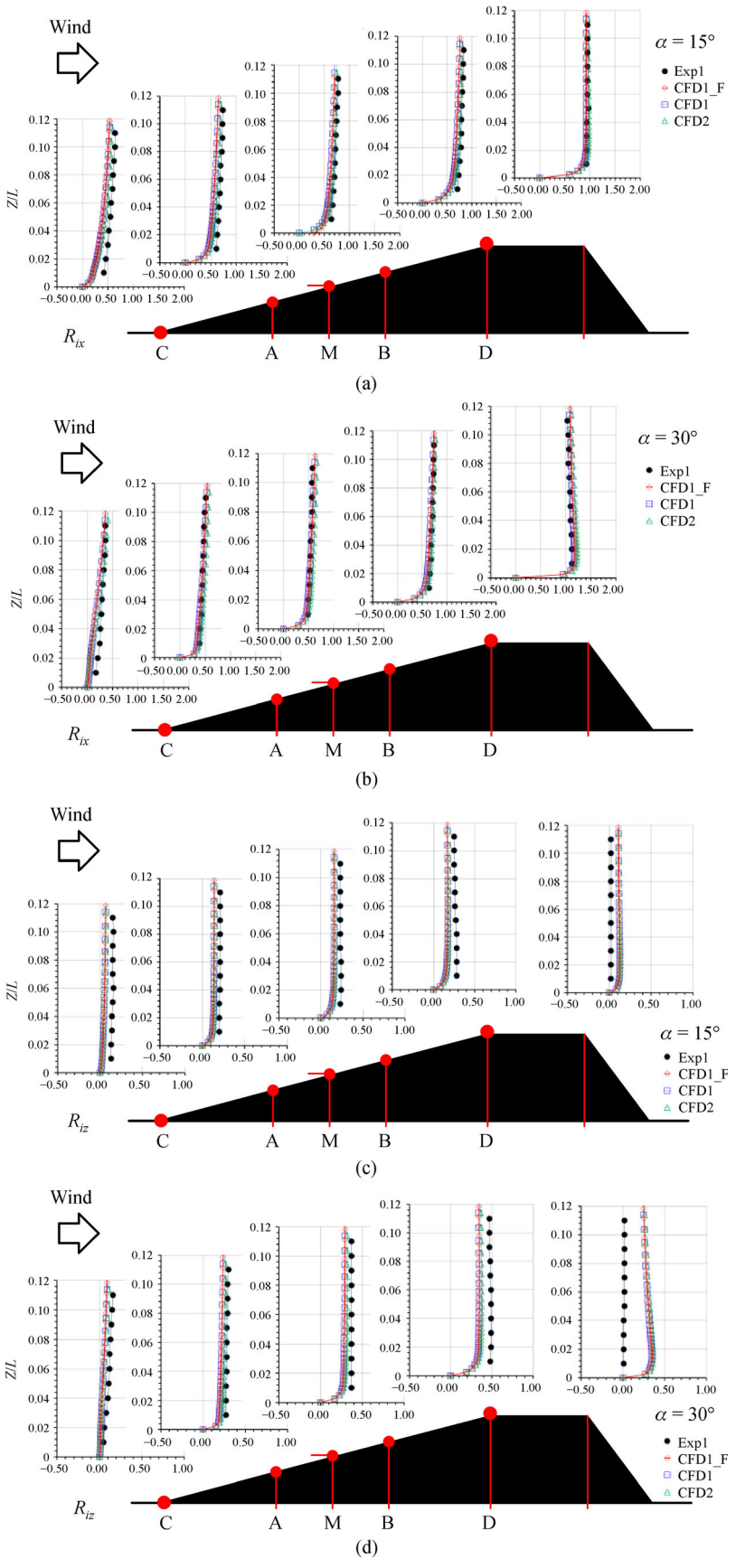


**Fig. 5** Comparisons of the wind speed ratios from the uphill terrain model with limited-length upper surface: (a) streamwise wind speed ratios for slope angle $\alpha = 15°$; (b) streamwise wind speed ratios for slope angle $\alpha = 30°$; (c) vertical wind speed ratios for slope angle $\alpha = 15°$; and (d) vertical wind speed ratios for slope angle $\alpha = 30°$.

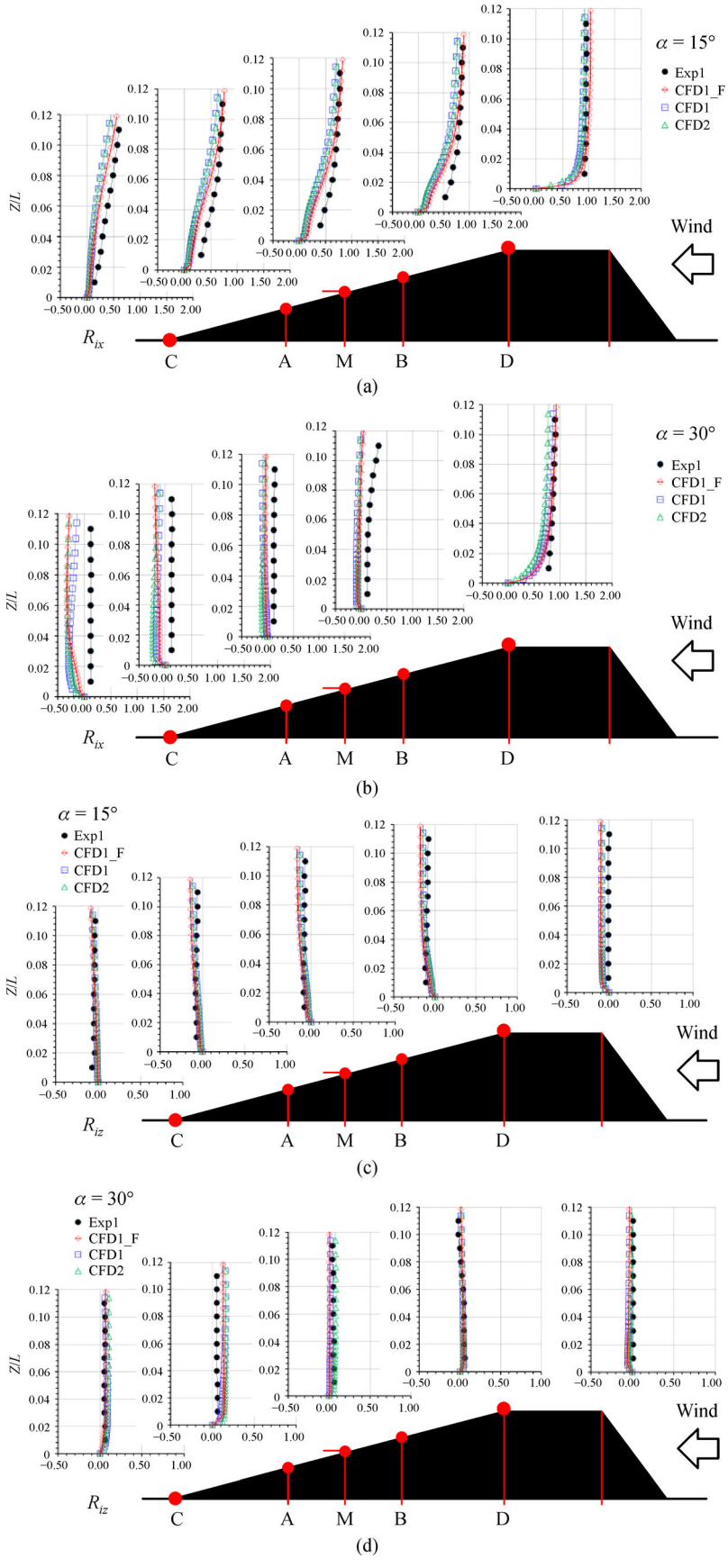


**Fig. 6** Comparisons of the wind speed ratios from the downhill terrain model with limited-length upper surface: (a) streamwise wind speed ratios for slope angle $\alpha = 15°$; (b) streamwise wind speed ratios for slope angle $\alpha = 30°$; (c) vertical wind speed ratios for slope angle $\alpha = 15°$; and (d) vertical wind speed ratios for slope angle $\alpha = 30°$.

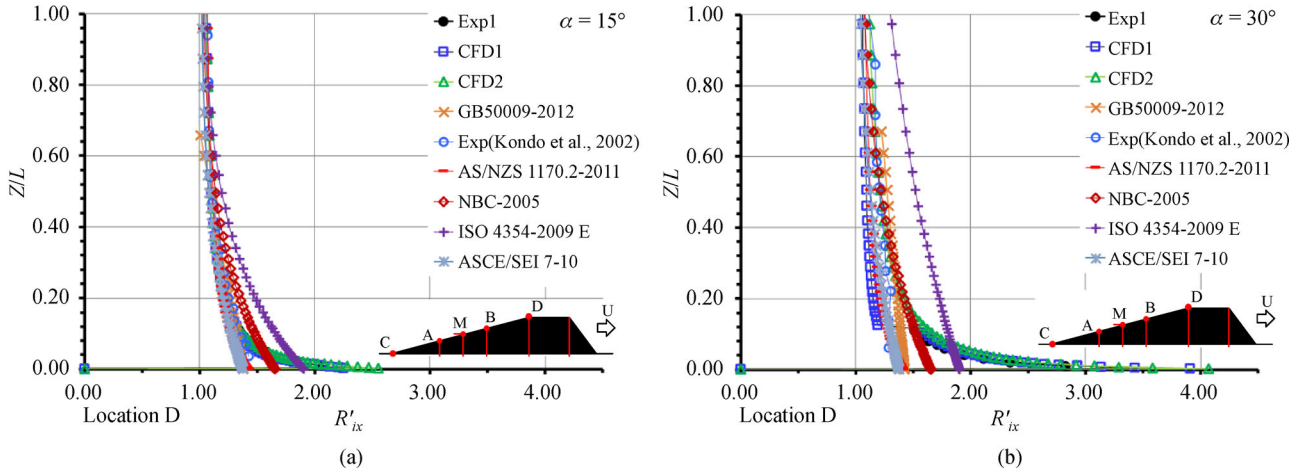


**Fig. 7** Comparisons of the topographic multiplier from the uphill terrain model with limited-length upper surface among the available results: (a) comparisons for the slope angle $\alpha = 15°$ and (b) comparisons for the slope angle $\alpha = 30°$.

four slope angles of $\alpha = 15°$, 30°, 45° and 60° were first simulated, as shown in Figs. 4–6 marked by "CFD2". It was found that there is almost no difference in the wind pressure coefficients and the wind speed ratios between "CFD1" and "CFD2". One of the main conclusions is that the horizontal length of $7L$ in the terrain model with a limited-length upper surface was long enough to approximate an ideal 2D terrain model. Another conclusion is that the CFD method can capture the main characteristics of the flow around the terrain model; thus, it can be used to investigate the aerodynamic characteristics of the ideal 2D terrain model with uniform incoming flow.

### 4.2 Effects of the slope angle on the wind pressure coefficients

Based on the validated CFD method with a uniform incoming flow of $U = U_g = 7.4$ m/s, the effects of the slope angle on the wind pressure coefficients around the ideal 2D terrain model were numerically simulated. The slope angle range was set from 5° to 60° with an interval of 5° for each simulation case. Figure 9 shows variations in the mean wind pressure coefficients with different slope angles for the ideal 2D terrain model. Similar trends exist at the locations of C, A, M and B for the uphill terrain model, as shown in Fig. 9(a). The wind pressure coefficients are all positive values and increase with increasing slope angle. For location D, where wind suction with negative pressure coefficients exists, a negative peak value with a slope angle of $\alpha = 40°$ exists. As shown in Fig. 9(b), descending trends can be observed for the wind pressure coefficients at locations C, A, M and B for the downhill terrain model. The wind pressure coefficients are mainly negative values for these four locations, except that positive wind pressure coefficients occur at locations C and A when $\alpha \leqslant 30°$. This might be caused by the reattachment flow induced by the flow separation at location D. The whole slope surface was immersed in the reattachment flow with increasing slope angle. There is also a negative peak value at location D with a slope angle of $\alpha = 30°$.

### 4.3 Effects of the slope angle on the wind speed ratios for the uphill terrain model

The simulation results of the streamwise and vertical wind speed ratios for the uphill model are shown in Figs. 10 and 11, respectively. Figure 10 shows that the streamwise wind speed ratios are mostly less than1.0 for the points above the ground at locations C, A, M and B. The ratios decrease gradually with increasing slope angle. However, the wind speed ratios are mostly greater than1.0 for the points above the ground at location D, where wind speed acceleration induced by the flow separation exists. More specifically, the wind speed ratios at the points above the ground at location D increase with increasing slope angle, reach their peak values at the slope angle of $\alpha = 40°$, and decrease when the slope angle increases further. For the vertical wind speed ratio shown in Fig. 11, the vertical wind speed ratios for all points above the ground basically increase with the slope angle when $\alpha \leqslant 40°$. The increasing trend remains for the points above the ground at locations M, B and D when the slope angle increases further. However, for the points above the ground at locations C and A, which are near the bottom of the terrain model, the vertical wind speed ratios appear to decrease. In particular, the vertical wind speed ratio becomes negative for points at location C, which is the same as that shown in Fig. 10(a). The negative values of the wind speed ratios indicate that the stagnation phenomenon occurs at the bottom of the slope surface when $\alpha \geqslant 50°$.

### 4.4 Effects of the slope angle on the wind speed ratios for the downhill terrain model

The simulation results of the streamwise and vertical wind speed ratios for the downhill model are shown in Figs. 12 and 13, respectively. Figure 12 shows that the streamwise

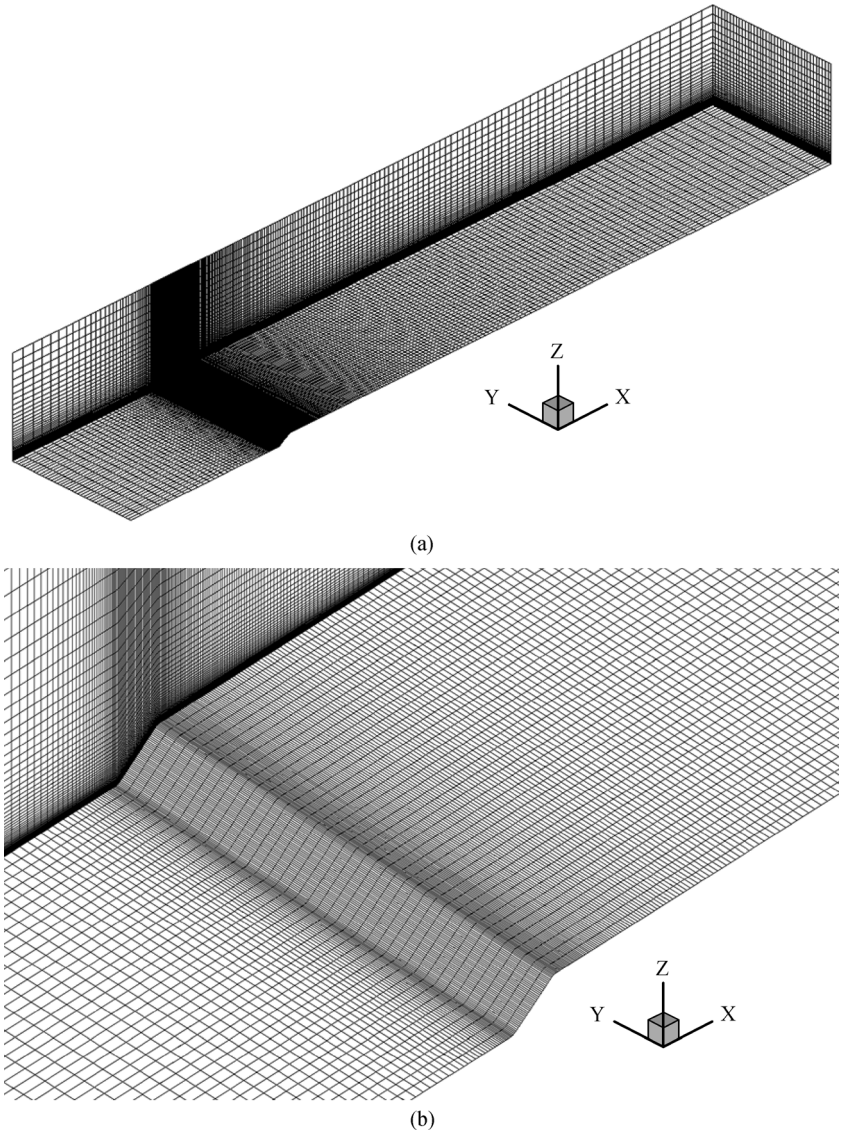


**Fig. 8** (a) Overview of the CFD domain and mesh scheme and (b) close view of the mesh scheme around the terrain model with unlimited-length upper surface.

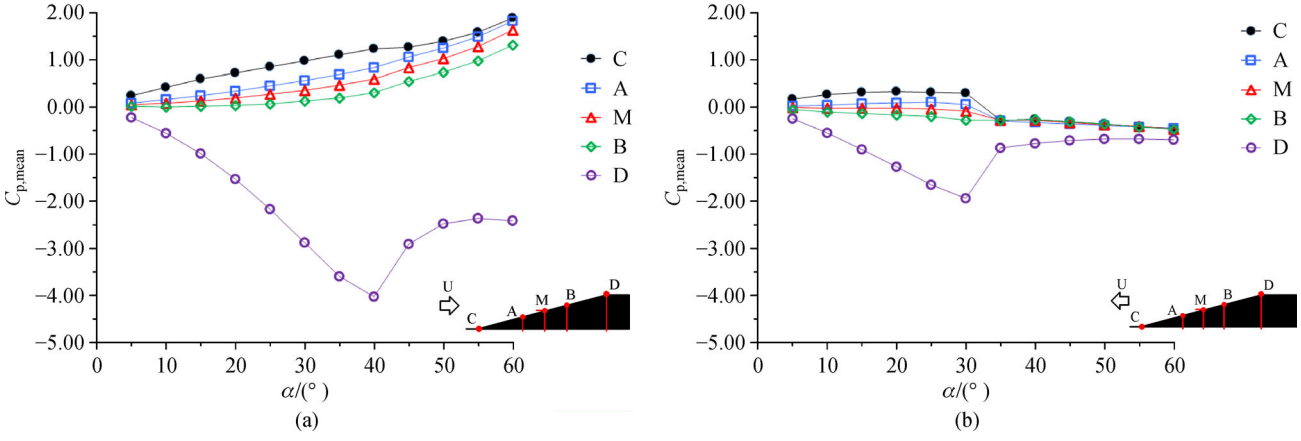


**Fig. 9** Variations in the mean wind pressure coefficients at locations along the slope surface with different slope angles for the ideal 2D terrain model with uniform incoming flow: (a) uphill terrain model and (b) downhill terrain model.

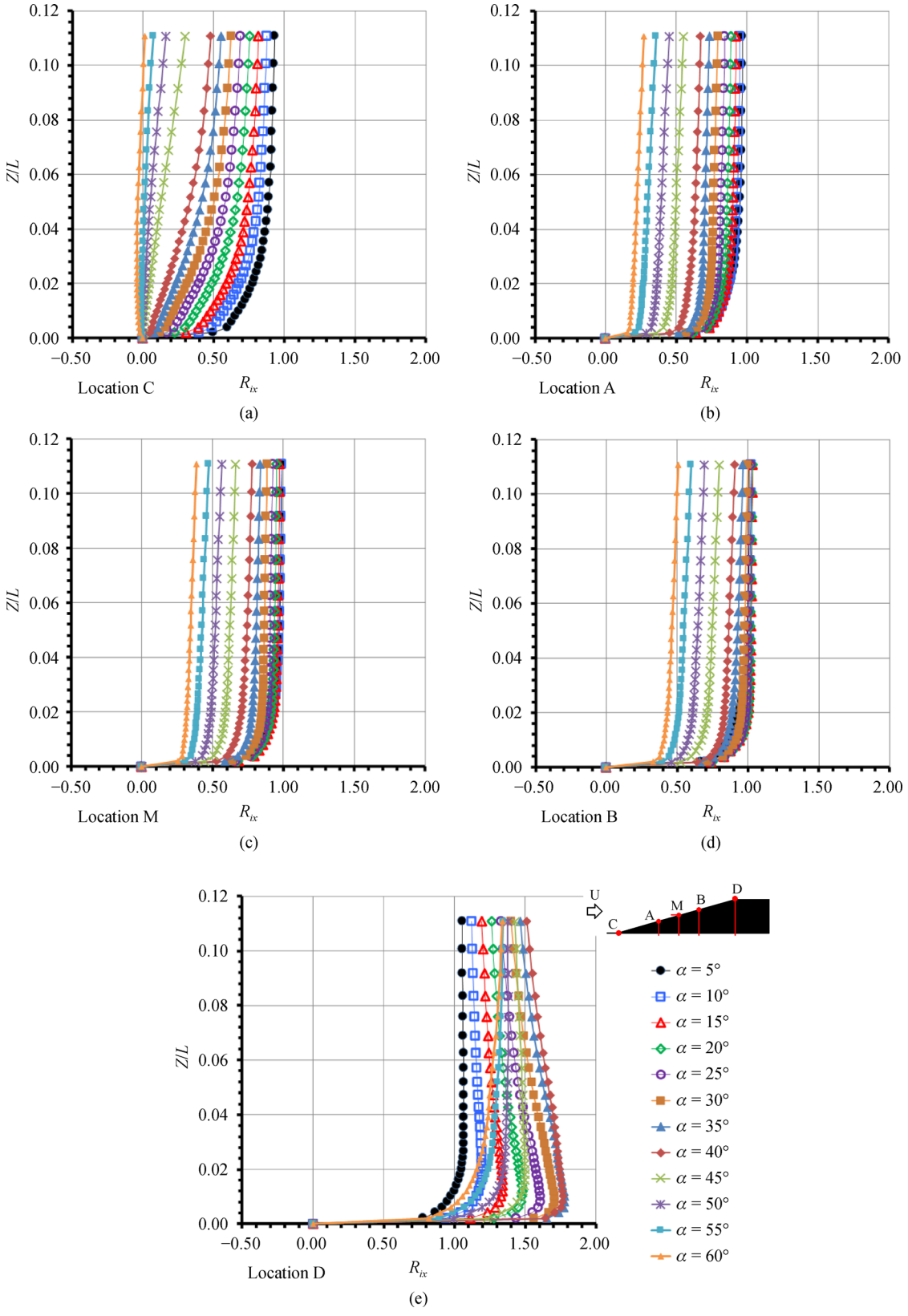


**Fig. 10** Variations in the streamwise wind speed ratios with the different slope angles for the 2D ideal uphill terrain model with uniform incoming flow.

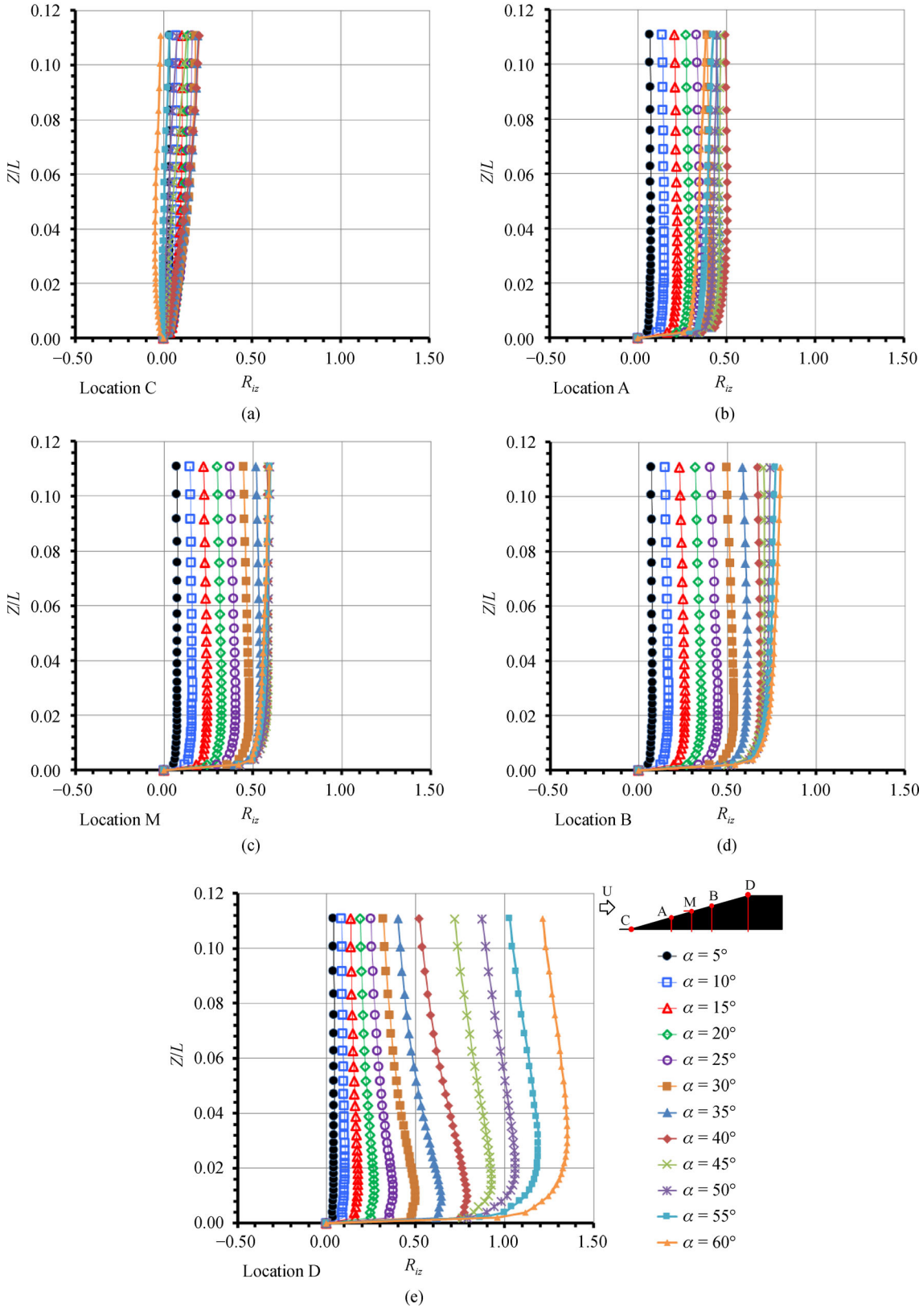


**Fig. 11** Variations in the vertical wind speed ratios with the different slope angles for the ideal 2D uphill terrain model with uniform incoming flow.

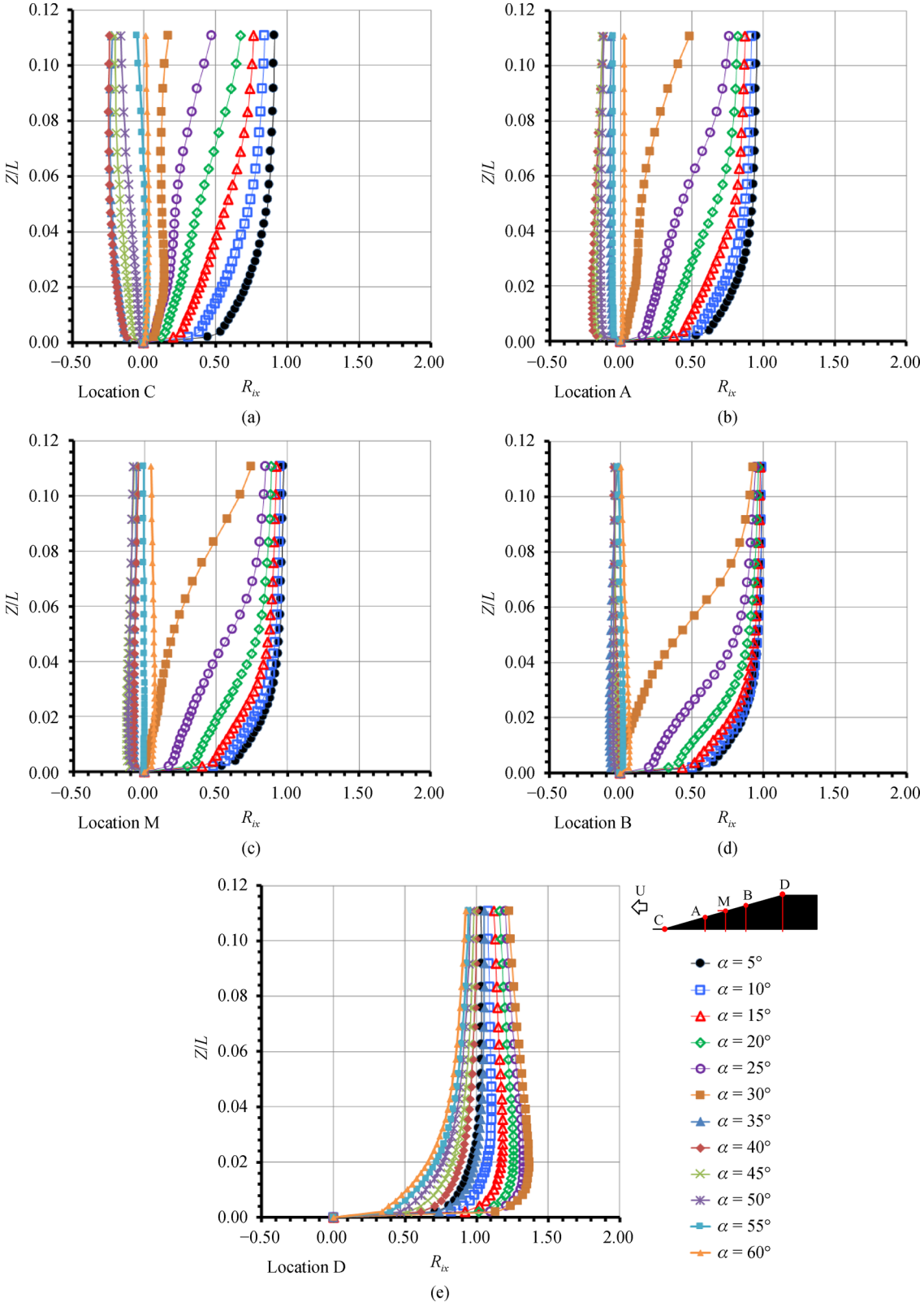


**Fig. 12** Variations in the streamwise wind speed ratios with the different slope angles for the ideal 2D downhill terrain model with uniform incoming flow.

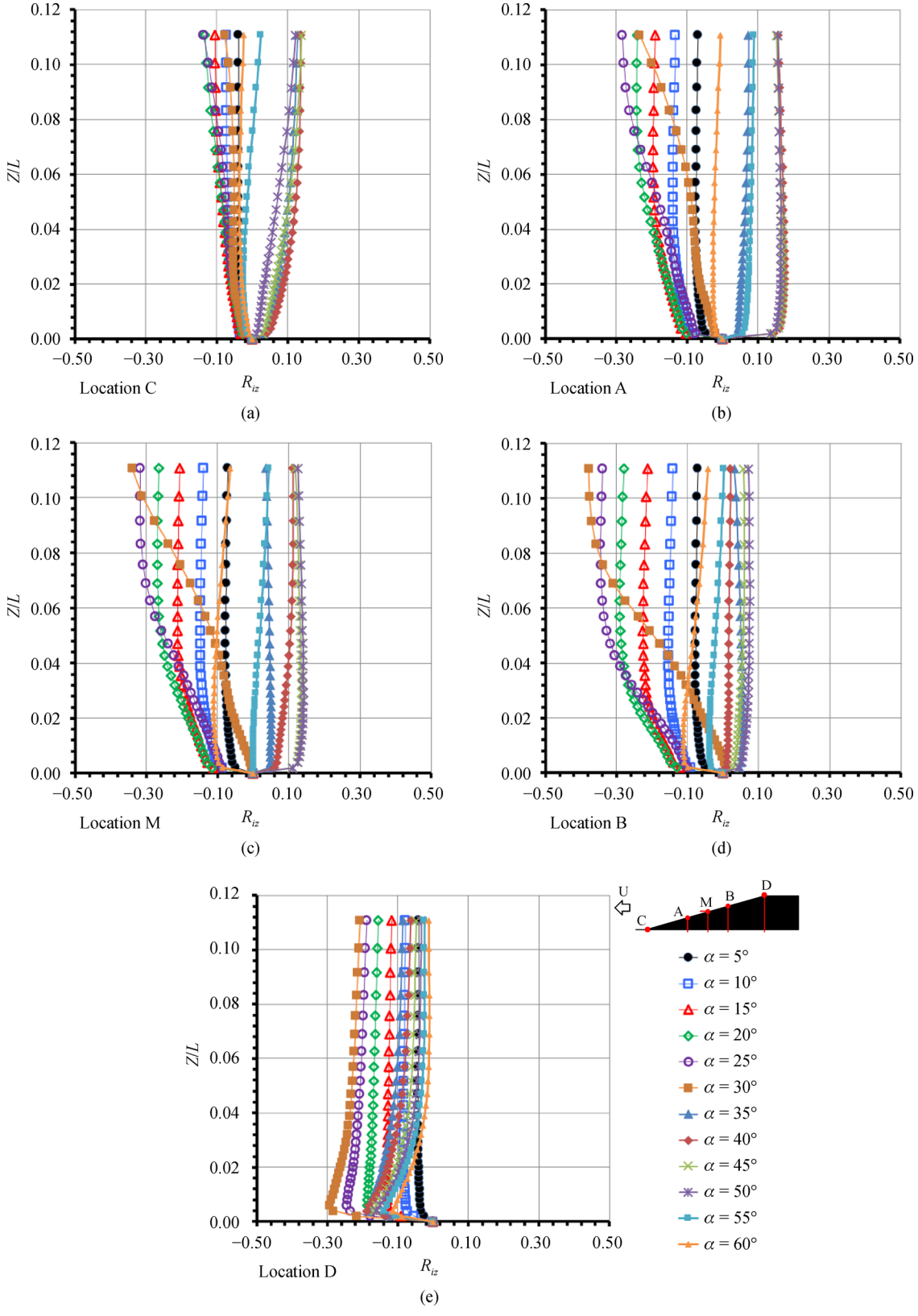


**Fig. 13** Variations in the vertical wind speed ratios with the different slope angles for the ideal 2D downhill terrain model with uniform incoming flow.

wind speed ratios are less than1.0 at the points above the ground at locations C, A, M and B. The ratios decrease with increasing slope angle and become negative at larger slope angles. It can also be seen that a critical slope angle of $\alpha = 30°$ exists where a negative wind speed ratio emerges, as is clearly shown at location B (Fig. 12(d)). For the points at location D (Fig. 12(e)), the streamwise wind speed ratios gradually increase with increasing slope angle, reach their peak values at the slope angle of $\alpha = 30°$, and decrease noticeably when the slope angle increases further (less than the values at the slope angle of $\alpha = 5°$). For the vertical wind speed ratios shown in Fig. 13, negative values are basically observed for all points, and the absolute values increase with the slope angle when $\alpha \leqslant 30°$. The ratios become positive and increase for the points above the ground at locations C, A, M, and B when the slope angle further increases and decrease again when $\alpha \geqslant 55°$; for the points above the ground at location D (Fig. 13(e)), the ratios remain negative and the absolute values decrease with increasing slope angle.

## 5 Discussion and conclusions

Aerodynamic characteristics around various 2D terrain models with different incoming flows were numerically and experimentally investigated. The results of the present study can provide basic aerodynamic information to calculate the wind field with finer resolution for a dynamical downscaling model and a parametric wind field model for typhoons, which were developed by the Shanghai Typhoon Institute. Some conclusions are as follows:

1) Aerodynamic characteristics around a 2D terrain model with a limited-length upper surface under the condition of the sheared incoming flow were studied by the wind tunnel and the numerical method. Special efforts were made to maintain the inflow boundary conditions throughout the computational domain. The computational results of the wind pressure coefficients and the streamwise and vertical wind speed ratios basically coincide with the experimental data, despite the difference in the estimation of the vertical wind speed ratios for the 2D uphill terrain model. The present numerical method is thus applicable in simulating the flow field around the 2D terrain models.

2) Based on the above validation, an ideal 2D terrain model with uniform incoming flow was studied by the numerical method. The wind pressure distribution along the terrain surface is affected by the slope angle. Different trends are observed at the slope surface and the escarpment point. In particular, negative peak values of the wind pressure coefficients exist at the escarpment point, where flow separation occurs, for the uphill and downhill terrain models with slope angles of 40° and 30°, respectively.

3) Wind speed ratios above the ideal 2D terrain surface are also affected by the slope angle. For the uphill terrain case, the streamwise wind speed ratios are mostly less than 1.0 at the points above the slope surface and decrease gradually with increasing slope angle. The ratios are greater than 1.0 for the points above the escarpment point. More specifically, the wind speed ratios at the points above the escarpment point increase with increasing slope angle, reach their peak values at a slope angle of 40°, and decrease when the slope angle increases further (but values are still larger than the values at a slope angle of $\alpha = 5°$).

4) For the downhill terrain model, the streamwise wind speed ratios are also less than 1.0 at the points above the slope surface. The ratios decrease with increasing slope angle and become negative values at larger slope angles. The streamwise wind speed ratios at the points above the escarpment point increase with increasing slope angle, reach their peak values at the slope angle of $\alpha = 30°$, and decrease noticeably when the slope angle increases further (less than the values at the slope angle of $\alpha = 5°$).

**Acknowledgements** The authors gratefully acknowledge the support of the Ministry of Science and Technology of China (Grant Nos. 2015CB452806 and 2018YFB1501104), the National Natural Science Foundation of China (Grant Nos. 51408196 and 41805088), the Natural Science Foundation of Shanghai (Grant No. 19ZR1469200) and the Young Backbone Teacher Cultivation Program of Henan University of Technology.

## References

Blocken B, Stathopoulos T, Carmeliet J (2007). CFD simulation of the atmospheric boundary layer: wall function problems. Atmos Environ, 41(2): 238–252

Bowen A J, Lindley D (1977). A wind-tunnel investigation of the wind speed and turbulence characteristics close to the ground over various escarpment shapes. Boundary-Layer Meteorol, 12(3): 259–271

Cao S, Tamura T (2006). Experimental study on roughness effects on turbulent boundary layer flow over a two-dimensional steep hill. J Wind Eng Ind Aerodyn, 94(1): 1–19

Cao S, Tamura T (2007). Effects of roughness blocks on atmospheric boundary layer flow over a two-dimensional low hill with/without sudden roughness change. J Wind Eng Ind Aerodyn, 95(8): 679–695

Cao S, Wang T, Ge Y, Tamura Y (2012). Numerical study on turbulent boundary layers over two-dimensional hills-effects of surface roughness and slope. J Wind Eng Ind Aerodyn, 104–106: 342–349

Cindori M, Juretic F, Kozmar H, Dzijan I (2018). Steady RANS model of the homogeneous atmospheric boundary layer. J Wind Eng Ind Aerodyn, 173: 289–301

COST Action 732 (2005–2009). Quality assurance and improvement of micro-scale meteorological models. Available at Hamberg University website

Dickinson R E, Errico R M, Giorgi F, Bates G T (1989). A regional climate model for the western United States. Clim Change, 15(3): 383–422

Fan L J (2006). Statistical downscaling of local and regional climate scenarios over china. Dissertation for Doctoral Degree. Beijing: Graduate School of Chinese Academy of Sciences (Institute of

Atmospheric Physics) (in Chinese)

Fang P Z, Gu M, Tan J G, Han Z H (2015). A method to solve the wall function problem in simulating the atmospheric boundary layer. Journal of Vibration and Shock, 34(2): 85–90 (in Chinese)

Hu W C, Yang Q S, Zhang J (2018). Comparative study on wind topographic factor of hilly terrain by different codes and standards. Engineering Mechanics, 35(10): 206–214 (in Chinese)

Ishihara T, Hibi K, Oikawa S (1999). A wind tunnel study of turbulent flow over a three-dimensional steep hill. J Wind Eng Ind Aerodyn, 83 (1–3): 95–107

Ishihara T, Fujino Y, Hibi K (2001). A wind tunnel study of separated flow over a two-dimensional ridge and a circular hill. J Wind Eng Ind Aerodyn, 89: 573–576

Ishihara T, Hibi K (2002). Numerical study of turbulent wake flow behind a three-dimensional steep hill. Wind Struct, 5(2–4): 317–328

Jackson P S, Hunt J C R (1975). Turbulent wind flow over a low hill. Q J R Meteorol Soc, 101(430): 929–955

Juretic F, Kozmar H (2014). Computational modeling of the atmospheric boundary layer using various two-equation turbulence models. Wind Struct, 19(6): 687–708

Kamada Y, Li Q, Maeda T, Yamada K (2019). Wind tunnel experimental investigation of flow field around two-dimensional single hill models. Renew Energ, 136: 1107–1118

Kondo K, Tsuchiya M, Sanada S (2002). Evaluation of effect of micro-topography on design wind velocity. J Wind Eng Ind Aerodyn, 90 (12–15): 1707–1718

Launder B E, Spalding D B (1974). The numerical computation of turbulent flows. Comput Methods Appl Mech Eng, 3(2): 269–289

Liu Z, Ishihara T, Tanaka T, He X (2016). LES study of turbulent flow fields over a smooth 3-D hill and a smooth 2-D ridge. J Wind Eng Ind Aerodyn, 153: 1–12

Lun Y F, Mochida A, Yoshino H, Murakami S (2007). Applicability of linear type revised $k$–$\varepsilon$ models to flow over topographic features. J Wind Eng Ind Aerodyn, 95(5): 371–384

Makridis A, Chick J (2013). Validation of a CFD model of wind turbine wakes with terrain effects. J Wind Eng Ind Aerodyn, 123(4): 12–29

Mortensen N G, Landberg L (1993). Wind Altas Analysis and Application Program (WASP) User's Guide. Roskilde, Denmark: Riso National Laboratory

Shih T H, Liou W W, Shabbir A, Yang Z, Zhu J (1995). A new eddy viscosity model for high Reynolds number turbulent flows model development and validation. Comput Fluids, 24(3): 227–238

Tominaga Y, Mochida A, Yoshie R, Kataoka H, Nozu T, Yoshikawa M, Shirasawa T (2008). AIJ guidelines for practical applications of CFD to pedestrian wind environment around buildings. J Wind Eng Ind Aerodyn, 96(10–11): 1749–1761

Van Doormaal J P, Raithby G D (1984). Enhancements of the SIMPLE method for predicting incompressible fluid flows. Numer Heat Tra-Appl, 7(2): 147–163

Walton D B, Sun F P, Hall A, Capps S (2015). A hybrid dynamical-statistical downscaling technique. Part I: development and validation of the technique. J Clim, 28(12): 4597–4617

Wang W, Shaw W J, Seiple T E, Rishel J P, Xie Y (2008). An evaluation of a diagnostic wind model (CALMET). J Appl Meteorol Climatol, 47(6): 1739–1756

Wilby R L, Wigley T M L (1997). Downscaling general circulation model output: a review of methods and limitations. Prog Phys Geogr, 21(4): 530–548

Wyngaard J C (2004). Toward numerical modeling in the "terra incognita". J Atmos Sci, 61(14): 1816–1826

Yan B W, Li Q S, He Y C, Chan P W (2016). RANS simulation of neutral atmospheric boundary layer flows over complex terrain by proper imposition of boundary conditions and modification on the $k$–$\varepsilon$ model. Environ Fluid Mech, 16(1): 1–23

Yang W, Andréasson J, Phil Graham L, Olsson J, Rosberg J, Wetterhall F (2010). Distribution-based scaling to improve usability of regional climate model projections for hydrological climate change impacts studies. Hydrol Res, 41(3–4): 211–229